European Journal of Chemistry 17 (2) (2026) 125-137

European Journal of Chemistry

Check for updates

View Journal Online
View Article Online

Toward an improved solid-state Li electrolyte: A first-principles investigation of the structure, Li-ion migration pathways, and ionic conductivity of $Li_7La_3Zr_2O_{12}$

Muhammad Mozammal Kamal Raju [1], Yulun Han [2], Dmitri Kilin [2,3,*], Yi Ding [4,*], and Qifeng Zhang [1,3,*]

[1] Department of Electrical and Computer Engineering, North Dakota State University, Fargo, ND 58108, USA
[2] Department of Chemistry and Biochemistry, North Dakota State University, Fargo, ND 58108, USA
[3] The Materials and Nanotechnology (MNT) Program, North Dakota State University, Fargo, ND 58105, USA
[4] Ground Vehicle Systems Center, Located (GVSC), US Army Combat Capabilities Development Command (DEVCOM), Warren, MI 48397-5000, USA

* Corresponding author at: Department of Electrical and Computer Engineering, North Dakota State University, Fargo, ND 58108, USA.
e-mail: dmitri.kilin@ndsu.edu (D. Kilin), yi.ding8.civ@army.mil (Y. Ding), qifeng.zhang@ndsu.edu (Q. Zhang).

RESEARCH ARTICLE

10.5155/eurjchem.17.2.125-137.2759

Received: 29 December 2025
Received in revised form: 15 March 2026
Accepted: 10 April 2026
Published online: 30 June 2026
Printed: 30 June 2026

KEYWORDS

Activation energy
Ionic conductivity
Molecular dynamics (MD)
Radial distribution function
Density functional theory (DFT)
Lithium lanthanum zirconium oxide (LLZO)

ABSTRACT

Among solid state electrolytes, garnet-type $Li_7La_3Zr_2O_{12}$ (LLZO) has attracted considerable attention due to its high electrochemical stability, safety, and compatibility with lithium metal anodes. However, its lithium-ion conductivity strongly depends on the crystal structure: the tetragonal phase exhibits a significantly lower ionic conductivity than the cubic phase. In this work, first-principles density functional theory (DFT) and ab initio molecular dynamics (AIMD) are employed to systematically investigate the crystallographic structure, lithium-ion migration pathways, and ionic conductivity of both tetragonal and cubic LLZO. Lithium ion trajectories were analysed to determine diffusion coefficients over a wide temperature range. Activation energies are extracted from Arrhenius behaviour, and room-temperature ionic conductivities are extrapolated from high-temperature simulations. The results reveal that cubic LLZO possesses an intrinsically disordered lithium sublattice with abundant vacant sites and shorter migration pathways, which significantly enhance lithium-ion mobility. Consequently, the extrapolated room temperature ionic conductivity of cubic LLZO reaches the order of ~10^{-3} S/cm, in good agreement with experimental reports, while tetragonal LLZO exhibits much lower conductivity. This study provides atomistic-level insight into lithium diffusion mechanisms in LLZO and offers guidance for designing high-performance garnet-type solid electrolytes through structural disorder and vacancy engineering.

Cite this: *Eur. J. Chem.* **2026**, *17(2)*, 125-137 **Journal website**: www.eurjchem.com

1. Introduction

With the rapid depletion of fossil fuel resources and the growing demand for sustainable energy technologies, the development of reliable and efficient energy storage systems has become a critical research focus over the past several decades. Among various energy storage technologies, lithium-ion batteries (LIBs) are considered one of the most promising candidates due to their high energy density, high power density, long cycle life, and portability [1]. However, conventional LIBs employing liquid electrolytes have safety concerns, such as flammability, leakage, and thermal instability, which limit their high-energy and large-scale applications.

To address these challenges, extensive research has been conducted inorganic solid-state electrolytes, which offer intrinsic advantages such as negligible self-discharge, superior chemical and thermal stability, compact size, environmental friendliness, increased safety, and improved reliability [2-4]. Rigorous research is underway on different types of solid-state inorganic electrolytes, namely garnet type LLZO [5-7], NASICON type [8,9], LISICON type [10,11], perovskite type [12,13], LIPON type [14], but most of them except garnet type LLZO cannot meet all the needs mentioned above, especially in terms of lithium ionic conductivity at room temperature and chemical stability with cathode and/or anode (Li metal).

$Li_7La_3Zr_2O_{12}$ (LLZO) is one of the most studied garnet-type solid electrolytes due to its favorable electrochemical properties. LLZO crystallizes in two distinct polymorphs: a tetragonal phase (space group $I4_1/acd$) and a cubic phase (space group $Ia\bar{3}d$). The tetragonal phase is thermodynamically stable at room temperature, but exhibits a relatively low lithium-ion conductivity of the order of ~10^{-7} S/cm [6,15]. In contrast to tetragonal phase LLZO (t-LLZO), the cubic phase LLZO (c-LLZO) exhibits a higher ionic conductivity on the order of ~10^{-3} S/cm [5,7,16]; generally, the transition temperature from the tetragonal phase to the cubic phase is in the range of 400 K to 650 K [16].

https://dx.doi.org/10.5155/eurjchem.17.2.125-137.2759

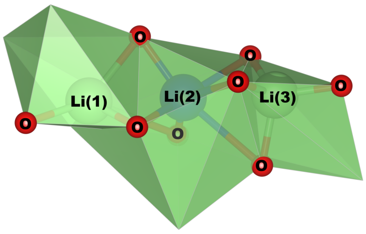

Figure 1. Polyhedral view of the octahedral and tetrahedral sites of LLZO. The octahedral site is constructed by a Li(2) (blue) atom with six O (red) atoms and the tetrahedral site is constructed by a Li(1) (green) or Li(3) (green) atom with four O atoms.

Understanding the microscopic mechanisms governing lithium ion diffusion in LLZO is essential for optimizing its ionic conductivity. First-principles density functional theory (DFT) and ab initio molecular dynamics (AIMD) simulations have proven to be a powerful approach to investigate ion transport mechanisms in solid electrolytes [17,18]. AIMD provides a reliable framework for capturing thermally activated bond breaking and bond formation processes, including reactions that require quantum mechanical descriptions [19-22]. The temperature dependence of average bond-breaking rates obtained from AIMD typically follows Arrhenius behavior. In addition, excited-state AIMD has been shown to successfully reproduce experimental trends in processes such as polymer photodegradation, photodecomposition of metal-organic complexes and photopolymerization, as well as in the fabrication of silicon and silicon carbide nanostructures [23-29]. In LLZO, lithium ions migrate via discrete hopping events between energetically favorable crystallographic sites. These sites are separated by potential energy barriers that determine the activation energy for lithium-ion diffusion. To successfully hop from one site to a neighboring site, a lithium ion must possess sufficient kinetic energy to overcome this barrier, such that $k_B T \geq E_a$, where $k_B$is the Boltzmann constant, T is the absolute temperature, and E_a is the activation energy. Consequently, the activation energy plays a central role in determining the lithium-ion conductivity of the material.

In the garnet structure, lithium ions occupy tetrahedral and octahedral coordination environments. As illustrated in Figure 1, a tetrahedral site is formed when a lithium ion is coordinated by four oxygen atoms, whereas an octahedral site is formed when a lithium ion is coordinated by six oxygen atoms. In this work, AIMD simulations are employed to analyze lithium-ion trajectories during migration in both tetragonal and cubic LLZO. Diffusion coefficients are calculated over a range of elevated temperatures, from which activation energies are extracted using Arrhenius analysis. Finally, the lithium-ion conductivity of LLZO at room temperature is extrapolated from the temperature-dependent diffusivity data.

2. Theory/Calculation

2.1. Electronic structure

The electronic structure calculations are performed within the framework of density functional theory (DFT) using the Kohn–Sham formalism, which provides an effective single-particle description of interacting electrons. The Kohn–Sham equations are written as (Equation 1) [30]

$$\left(-\hbar^2/_{2m}\nabla^2 + v\left[\{\vec{R}_I\},\vec{r},\rho(\vec{r})\right]\right)\varphi_i^{KS}(\{\vec{R}_I\},\vec{r}) = \varepsilon_i(\{\vec{R}_I\})\varphi_i^{KS}(\{\vec{R}_I\},\vec{r}) \quad (1)$$

where the first term represents the electronic kinetic energy operator and $\nabla = (\frac{\partial}{\partial x},\frac{\partial}{\partial y},\frac{\partial}{\partial z})$.

In Equation 1, one can find the set of one-electron orbital's $\varphi_i^{KS}(\{\vec{R}_I\},\vec{r})$and their energies, ε_i. The orbitals and their energies parametrically depend on nuclear position $\{\vec{R}_I\}$. The orbitals are combined with orbital occupation function (f_i) to construct the total density of electrons (Equation 2).

$$\rho(\vec{r}) = \sum_i f_i \varphi_i^{KS^*}(\vec{r})\varphi_i^{KS}(\vec{r}) \quad (2)$$

Note that the density consists of pairs of orbitals that share the same indices. The total electron density determines the effective potential, which is defined as the functional derivative of the total energy with respect to variations in the electron density. This potential includes the electron–ion interaction as well as electron–electron interactions, namely the Coulomb, exchange and correlation contributions (Equation 3).

$$v[\vec{r},\rho] = \delta/\delta\rho(E^{tot}[\rho] - T[\rho]) \quad (3)$$

In Equation 3, we symbolize functionality of the effective potential on the electron density. Equations 1-3 were solved self-consistently in an iterative manner using the VASP within the framework of the Perdew–Burke–Ernzerhof (PBE) exchange–correlation functional, although other functionals could also be employed [31,32].

2.2. Heating

The heating algorithm adjusts the system temperature by reheating or cooling it depending on whether the average atomic momentum is lower than or higher than the target value. Following the initial structural optimization using DFT within the VASP package, the system is gradually heated to the desired temperature, thereby increasing its kinetic energy to reach thermal equilibrium. The atomistic system is coupled to a thermostat at the chosen temperature by rescaling the atomic momenta, $\vec{P}_I$, for every time step $\sum_I^{N_I}\frac{\vec{P}_I^2}{2M_I} = \frac{3}{2}N_I k_B T$ (Equation 4)

$$\sum_{I=1}^{N}\frac{M_I\left(\frac{d\vec{R}_I}{dt}|_{t=0}\right)^2}{2} = \sum_{I=1}^{N}\frac{(\vec{P}_I)^2}{2M_I} = \frac{3}{2}Nk_B T \quad (4)$$

where M represents the ionic mass, N denotes the total number of ions, and k_B stands for the Boltzmann constant with units of eV/K.

The system is subsequently propagated for an infinitesimal time step to allow redistribution between the kinetic and potential energy components. This procedure is repeated iteratively until the kinetic energy stabilizes around the target value. The final configuration obtained after the heating stage is then used as the initial condition for subsequent molecular dynamics (MD) simulation. The momenta $\{\vec{P}_I(t)\}$ and positions $\{\vec{R}_I(t)\}$ obtained at the final step of the heating stage are used as the initial conditions for the subsequent molecular dynamics simulations.

2.3. Molecular dynamics

Following the heating step, the molecular dynamics simulation is performed. After the system reaches thermal stability, the equilibrated atomic momenta are employed to compute the adiabatic ground state trajectory through integration of Newton's equations of motion (Equation 5):

$$\frac{d^2}{dt^2}\vec{R}_I = \vec{F}_I([\rho(\vec{r})])/M_I \tag{5}$$

where $\vec{R}_I(t)$ represents the trajectory of each ion, obtained by integrating Newton's equation of motion with initial conditions taken from the heating stage. In AIMD, at each step, the Force $\vec{F}_I(t)$ is evaluated from the electronic structure using the Hellman Feynman theorem.

The diffusion properties were calculated by analyzing the lithium-ion trajectories $R_I(t)$, extracted from the simulations. The displacement ΔR_I of ion I from time, t_1 to t_2 is given by (Equation 6),

$$\Delta R_I(\Delta t) = \left|\vec{R_I}(t_2) - \vec{R_I}(t_1)\right| \\ = \sqrt{[x_I(t_2) - x_I(t_1)]^2 + [y_I(t_2) - y_I(t_1)]^2 + [z_I(t_2) - z_I(t_1)]^2} \tag{6}$$

where $\Delta t = t_2 - t_1$ is the time interval.

In solid electrolytes, lithium ions are primarily bound to crystallographic sites and migrate via discrete hopping events rather than continuous motion. At a given temperature, an ion must acquire sufficient kinetic energy to overcome the activation barrier and hop to a neighboring site. The characteristic time associated with the first successful hop is called the rise time, τ. The hopping rate, X, is defined as reciprocal of rise time (Equation 7):

$$X = \frac{1}{\tau} \quad \Rightarrow \log X = \log\frac{1}{\tau} \tag{7}$$

The hopping rates are evaluated at different temperatures over a simulation time of 50 ps. Assuming Arrhenius behavior, the temperature dependence of the hopping rate is expressed as Equation 8:

$$X(T) = \mathrm{A}\exp\left(\frac{-E_a}{k_BT}\right) \tag{8}$$

where A denotes the preexponential factor, T is the absolute temperature, and E_a denotes the corresponding activation energy.

When $X_1(T_1)$ and $X_2(T_2)$ are available, then the activation energy E_a can be evaluated using Equation 9:

$$E_a = -k_B\frac{\ln X_2(T_2) - \ln X_1(T_1)}{\frac{1}{T_2} - \frac{1}{T_1}} \tag{9}$$

The total squared displacement for N mobile ions is calculated over Δt time interval as $\sum_{i=1}^{N}\langle|\Delta R_I(\Delta t)|^2\rangle$, where $\langle[R(\Delta t)]^2\rangle$ represents the square displacement for corresponding Li ions. This quantity describes the collective motion of all N mobile ions over a time interval Δt. The total mean square displacement (TMSD) of the diffusing ions is calculated as Equation 10:

$$\mathrm{TMSD}(\Delta t) = \sum_{i=1}^{N}\langle|R_I(\Delta t) - R_I(0)|^2\rangle \tag{10}$$

The mean square displacement (MSD) is obtained from the time-averaged mean square displacement (TMSD) of each mobile ion (Equation 11):

$$\mathrm{MSD}(\Delta t) = \frac{1}{N}\,\mathrm{TMSD}(\Delta t) \tag{11}$$

The lithium-ion self-diffusion coefficient D, is calculated from the averaged mean square displacement based on the Einstein relation, expressed as follows (Equation 12):

$$D = \frac{\mathrm{MSD}(\Delta t)}{2d(\Delta t)} \tag{12}$$

Here, d = 3 represents the dimensionality of the lattice in which diffusion occurs. Subsequently, the ionic conductivity is calculated from the diffusivity D, using the Nernst–Einstein relationship (Equation 13) [33,34]:

$$\sigma = \frac{Nq^2D}{Vk_BT} \tag{13}$$

where V represents the total volume of the cell and q denotes charge of the ion species.

2.4. Radial distribution function

The radial distribution function (RDF), or pair correlation function, describes the spatial variation of the ionic density around a selected reference ion. Quantitatively, it represents the likelihood of finding neighboring ions at specific radial distances within the system.

The atomic positions, $\vec{R}_I(t)$, are recorded at every step along the molecular dynamics trajectory, enabling subsequent single-point electronic structure calculations. During thermal equilibration, structural modifications may occur, potentially promoting adsorption, desorption, or bond formation processes. To analyze local structural evolution, the radial distribution functions (RDF) are computed for selected atomic pairs throughout the MD simulation (Equation 14).

$$RDF(t,r) = \frac{1}{4\pi r^2}\sum_{IJ}\delta\left(r - \left|\vec{R}_I(t) - \vec{R}_J(t)\right|\right) \tag{14}$$

where $\vec{R}_I(t)$ and $\vec{R}_J(t)$ represent the I-th and J-th ion's position, respectively.

2.5. Computational details

Vienna *Ab initio* Simulation Package (VASP) is used in this study to perform first-principles calculations, employing a plane-wave basis set [35,36]. The interaction between valence and core electrons was described using the projector augmented wave (PAW) approach [37]. All simulations were performed using a plane wave cutoff energy of 520 eV, which was verified to provide well-converged total energies.

Exchange-correlation interactions were treated within the generalized gradient approximation using the Perdew–Burke–Ernzerhof (PBE) functional [31,32,38]. Brillouin zone sampling was carried out using the Monkhorst–Pack scheme. Structural visualization and analysis were performed using crystallographic data obtained from the Crystallography Open Database (COD) and the Materials Project.

For both cubic and tetragonal LLZO, supercells (*i.e.*, per formula unit, or pfu) containing eight formula units were constructed, corresponding to the stoichiometry $Li_{56}La_{24}Zr_{16}O_{96}$ and a total of 192 atoms as shown in Figure 2. The cubic LLZO structure was obtained from the COD entry 7206766, while the tetragonal LLZO structure was taken from the Materials Project entry mp-942733. In both structures, lithium ions are coordinated by either four or six oxygen atoms, whereas La^{3+} and Zr^{4+} ions occupy eightfold and sixfold oxygen coordination environments, respectively [39,40].

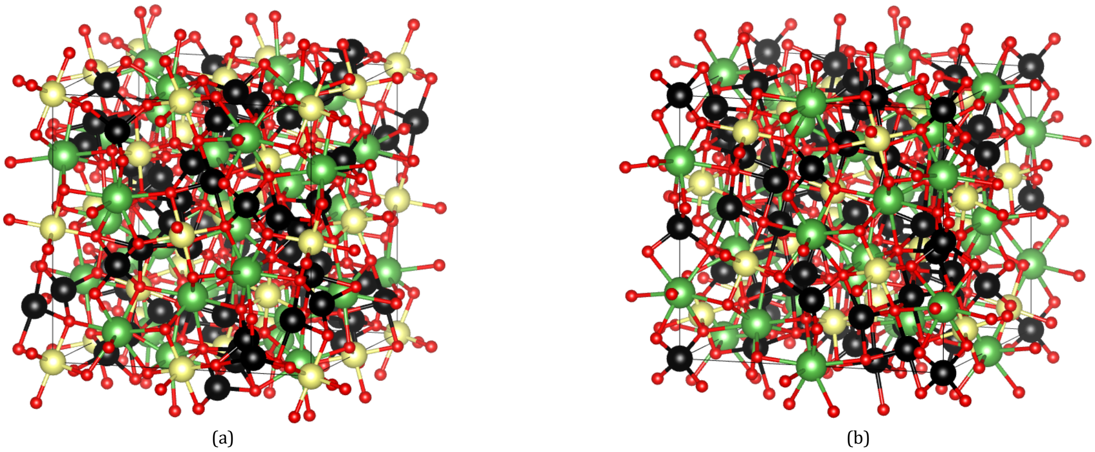
(a) (b)

Figure 2. Initial unit cell of (a) cubic and (b) tetragonal LLZO ($Li_{56}La_{24}Zr_{16}O_{96}$); red, green, yellow and black spheres represent oxygen (O), lanthanum (La), Zirconium (Zr) and lithium (Li), respectively; in which La and Zr ions are located in the center of dodecahedrons and octahedrons, respectively, and O atoms form polyhedrons with La and Zr ions, as shown in Figure S1.

Although the crystal structures contain intrinsic voids, overall charge neutrality and stoichiometric balance are preserved by the stable La–Zr–O framework, with lithium ions occupying available interstitial sites. In the cubic LLZO model, partial lithium site occupancies were implemented using site occupancy factors (SOFs) of g = 0.42 (24d tetrahedral sites) and g = 0.48 (6h octahedral sites), reflecting the experimentally observed disorder. In contrast, for tetragonal LLZO, full occupancy (g = 1) was assumed for lithium sites, including tetrahedral 8a and octahedral 16f and 32g positions.

3. Results and Discussion

3.1. Geometric structure and site changing

Garnet-type LLZO ($Li_7La_3Zr_2O_{12}$) belongs to the $Li_7A_3B_2O_{12}$ garnet family (A = La with other elements like Ga, Al or B = Zr with Ta), where lithium ions occupy both tetrahedral and octahedral interstitial sites, A-site cations reside in eightfold coordination environments, and B-site cations occupy sixfold coordinated sites. LLZO exists in two crystallographic phases. The material crystallizes either in a tetragonal structure (space group $I4_1/acd$), characterized by lattice parameters $a = b \neq c$ with α = β = γ = 90°, or in a cubic structure (space group $Ia\bar{3}d$), where $a = b = c$ and all interaxial angles are 90°. The arrangement and site occupancy of lithium ions within these two crystal frameworks critically influence the resulting lithium-ion conductivity.

In the tetragonal phase, lithium ions occupy three distinct crystallographic sites: the tetrahedral 8a sites and the octahedral 16f and 32g sites [6]. On the contrary, cubic LLZO contains only two types of lithium sites: tetrahedral 24d sites and octahedral 96h sites [7]. As a consequence, lithium ions in cubic LLZO have access to a significantly larger number of available sites for migration compared to those in tetragonal LLZO.

For an eight-per formula unit (pfu) LLZO supercell containing 56 lithium ions, the tetragonal phase provides exactly 56 available sites for lithium (8a, 16f, and 32g), resulting in a fully occupied and ordered lithium sublattice. On the contrary, the cubic phase offers a total of 120 lithium sites (24d and 96h) for the same number of lithium ions. This leaves 64 vacant sites in the cubic structure, which greatly facilitates lithium-ion migration. Awaka *et al.* reported that, in cubic LLZO, lithium ions predominantly occupy the 24d tetrahedral sites, while the higher-capacity octahedral sites remain partially vacant, allowing frequent lithium-ion hopping events [6].

Figure 3 illustrates the atomic configurations of cubic and tetragonal LLZO before and after AIMD simulations performed at 1500 K. Structural changes are primarily associated with lithium-ion migration, while the La–Zr–O framework remains largely intact. The trajectory of a representative lithium ion, Li(54), is highlighted by a blue sphere. In cubic LLZO, Li(54) initially resides near the upper left region of the simulation cell and migrates to a position near the bottom of the lattice after the simulation. In tetragonal LLZO, Li(54) also undergoes a positional change, moving from the upper left region to an opposite edge of the simulation cell.

The site occupancy of Li(54) before and after the AIMD simulation is further illustrated in Figure 4. In cubic LLZO, Li(54) initially occupies a tetrahedral 24d site (Figure 4a) and migrates to an octahedral 96h site after simulation (Figure 4b). On the contrary, in tetragonal LLZO, Li(54) initially occupies an octahedral site (Figure 4c) and migrates to another octahedral site following the simulation (Figure 4d). The total displacement of Li(54) during the AIMD simulation is provided in Figure S2.

Lithium-ion migration pathways differ markedly between cubic and tetragonal LLZO because of their distinct site topologies. In cubic LLZO, lithium ions can undergo transitions between tetrahedral and octahedral sites (24d ↔ 96h) as well as between neighboring octahedral sites (96h ↔ 96h), as illustrated in Figure 5a. Transitions between tetrahedral sites (24d ↔ 24d) are rarely observed at temperatures between 750 and 1500 K because of the relatively large separation between these sites. Only at higher temperatures do occasional 24d-to-24d transitions occur when lithium ions acquire sufficient kinetic energy to overcome the larger activation barriers (Figure S3). The increase in temperature enhances the thermal energy available to lithium ions, thereby increasing the probability of successful hopping events, including transitions over longer migration pathways. These observations are consistent with previous computational studies [41-43].

In tetragonal LLZO, lithium ions occupy three types of sites (8a, 16f, and 32g), enabling a greater number of nominal transition pathways (Figure 5b). However, due to the complete occupation of all lithium sites and the larger intersite distances, particularly between tetrahedral 8a sites (≈3.65 Å), successful lithium-ion hopping events are relatively infrequent. Consequently, transitions between tetrahedral sites are rarely observed, while migration predominantly occurs between neighboring octahedral sites (16f ↔ 32g). This behavior is illustrated in Figure 6b.

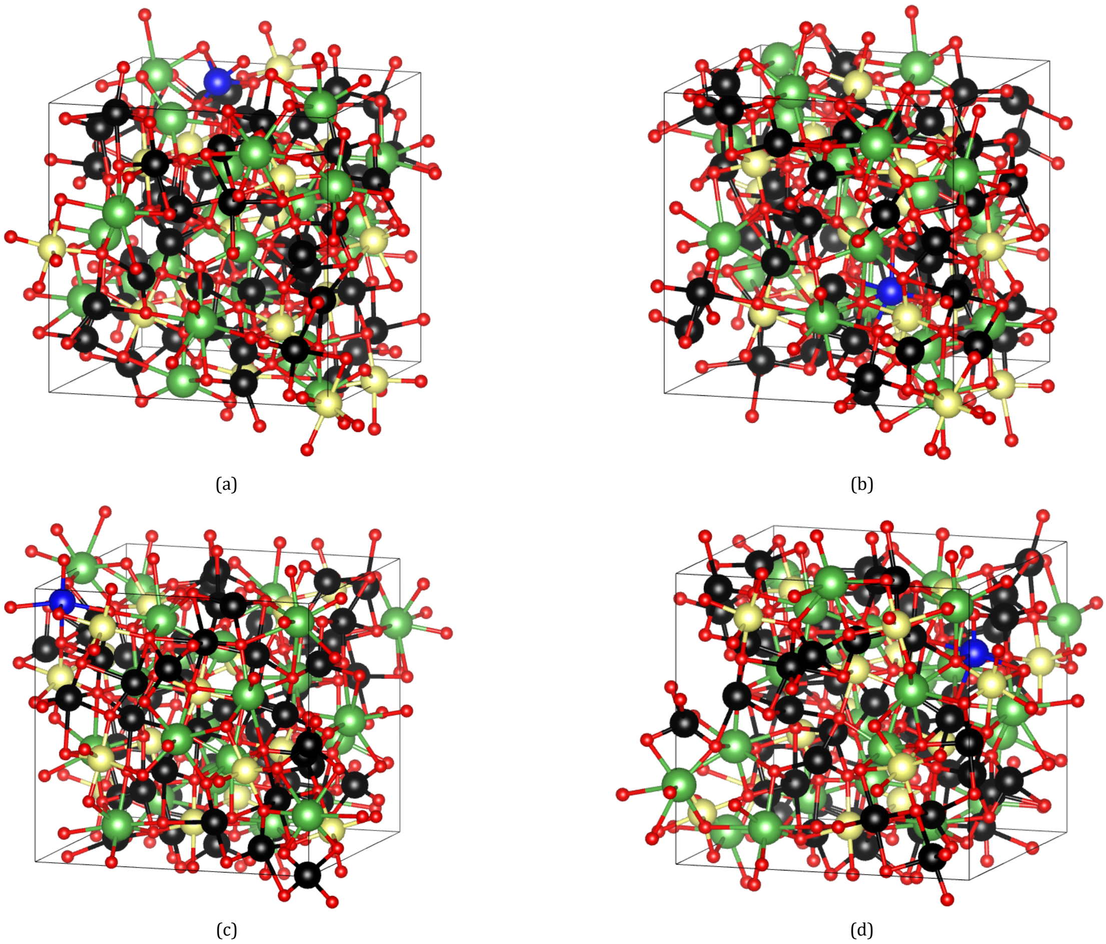

Figure 3. Structures of cubic LLZO (a)-(b) and tetragonal LLZO (c)-(d), where (a), (c) exhibit atomic positions before MD simulation and (b), (d) exhibit atomic positions after MD simulation at 1500 K, in which black spheres represent Li ions while the Li(54) ion is marked in blue.

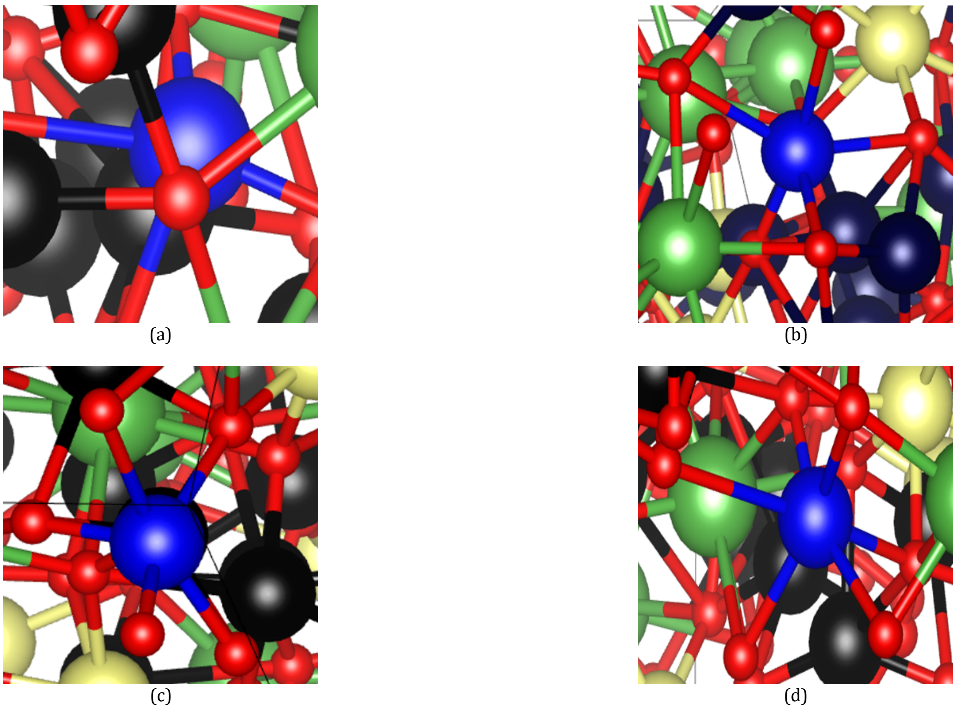

Figure 4. Site occupancy of the Li(54) ion before and after MD simulation at 1500 K. (a), (b) in cubic LLZO and (c), (d) in tetragonal LLZO.

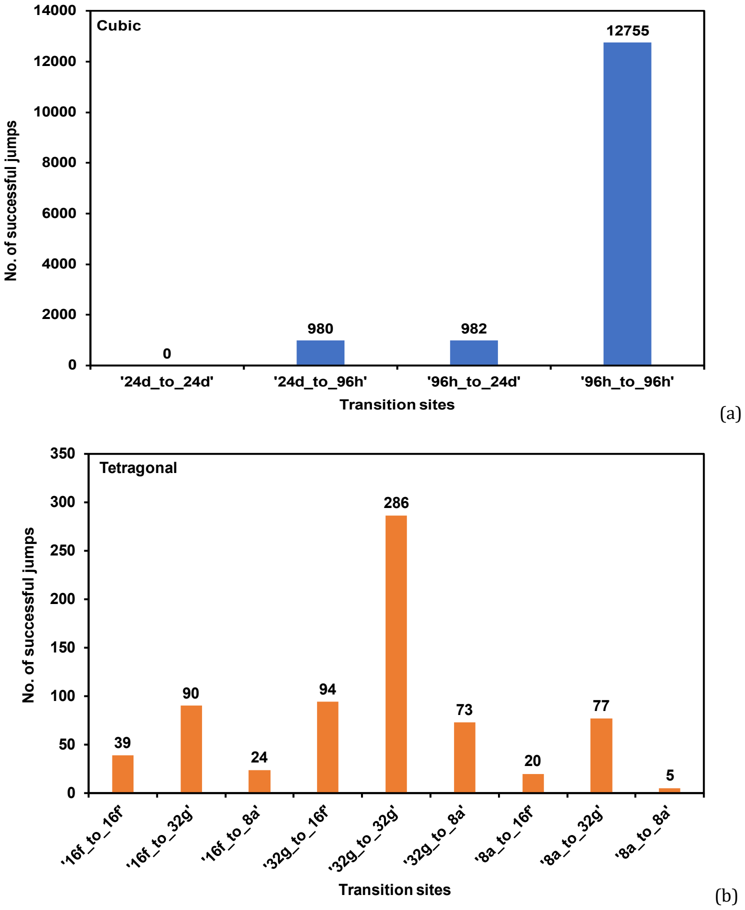

Figure 5. Numbers of successful jumps between different sites for (a) cubic LLZO and (b) tetragonal LLZO, respectively, after MD simulation at 1500 K.

Although cubic LLZO offers fewer distinct site-to-site transition types than tetragonal LLZO, the total number of successful lithium-ion jumps observed during AIMD simulations is substantially higher, as shown in Figure 6. This enhanced migration in cubic LLZO can be attributed to the shorter distances between neighboring octahedral 96h sites and the presence of abundant vacant sites, which promote rapid lithium ion hopping. On the fully occupied and ordered lithium sublattice in tetragonal LLZO restricts ion migration, leading to predominantly collective hopping events in which one lithium ion can move only when a neighboring ion vacates its site [7,43]. A schematic diagram to highlight the differences in migration pathways between the cubic and tetragonal phases is shown in Figure 7. These results demonstrate that disordered lithium sublattice and a higher vacancy concentration in cubic LLZO play a critical role in facilitating lithium ion transport, thereby explaining its significantly higher ionic conductivity compared to the tetragonal phase.

3.2. Molecular dynamics

The AIMD simulations reveal that lithium-ion motion in LLZO strongly depends on temperature and crystal structure. At relatively low temperatures, lithium ions primarily undergo localized vibrational motion around their equilibrium lattice sites. As the temperature increases, individual lithium ions gradually acquire sufficient kinetic energy to overcome the activation barriers that separate neighboring sites, leading to discrete hopping events. These hops may occur either individually (solo jumps) or cooperatively through correlated motion involving multiple ions. It should be noted that AIMD simulations are inherently limited by accessible time scales and computational cost. In the present work, we used a 50 ps trajectory and employed the temperature range 750–2000 K, which ensured necessarily sufficient lithium ion migration events within feasible simulation times.

Figure 8 schematically illustrates possible lithium-ion migration pathways in LLZO. Lithium ions occupying tetrahedral sites [Li(1) or Li(3)] can migrate to adjacent octahedral sites [Li(2)], provided that the destination site is vacant and the ion possesses sufficient kinetic energy to overcome the activation barrier. Similarly, lithium ions residing in octahedral sites can migrate to nearby tetrahedral sites if vacancies are available. Direct transitions between tetrahedral sites are not observed in cubic LLZO, consistent with the large separation between 24d sites and the corresponding high activation barriers.

The total number of successful lithium-ion hopping events observed during AIMD simulations at various temperatures is summarized in Figure 9 for both cubic and tetragonal LLZO. At all simulated temperatures, the cubic LLZO exhibits a substantially higher number of successful jumps than the tetragonal LLZO. This behavior reflects the lower activation barriers and greater availability of vacant sites in the cubic structure, which facilitate frequent lithium ion migration.

Figure 10 further distinguishes between collective and solo hopping events. In both cubic and tetragonal LLZO, the majority of successful hops occur through collective motion, in which multiple lithium ions move in a coordinated manner. This collective behavior arises because a lithium ion can occupy a neighboring site only when that site is either vacant or simultaneously vacated by another ion. Jump histograms obtained at 1500 K (Figure S4) further confirm the prevalence of collective hopping events. At 1500 K, cubic LLZO exhibits a consistently higher number of lithium-ion jump events throughout the simulation compared to tetragonal LLZO.

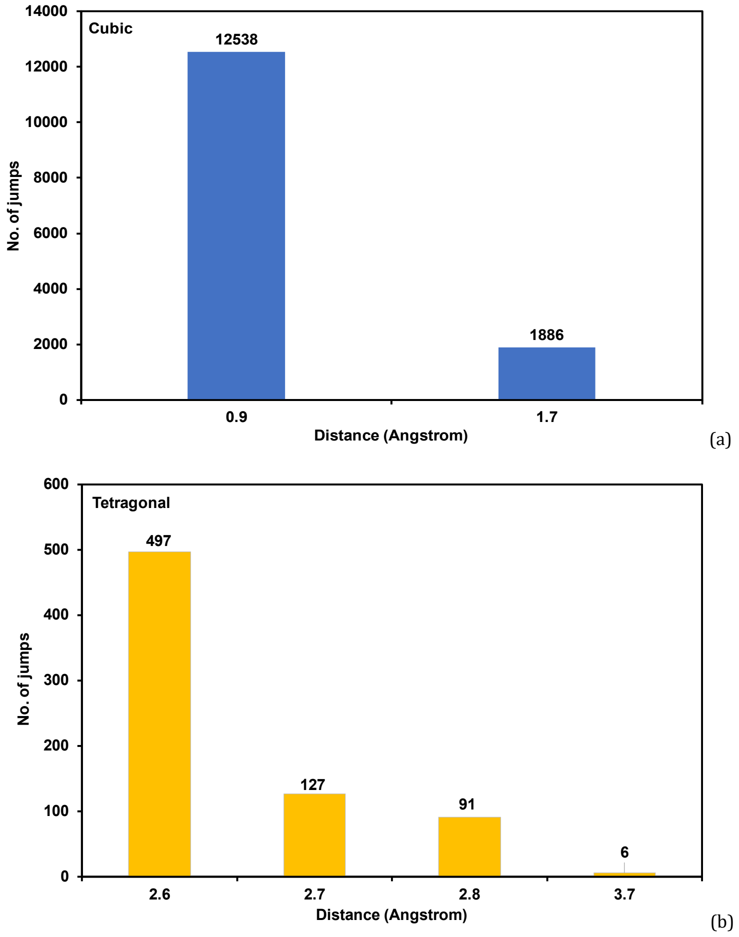

Figure 6. Successful jumps in (a) cubic LLZO and (b) tetragonal LLZO, respectively, under MD conditions at 1500 K.

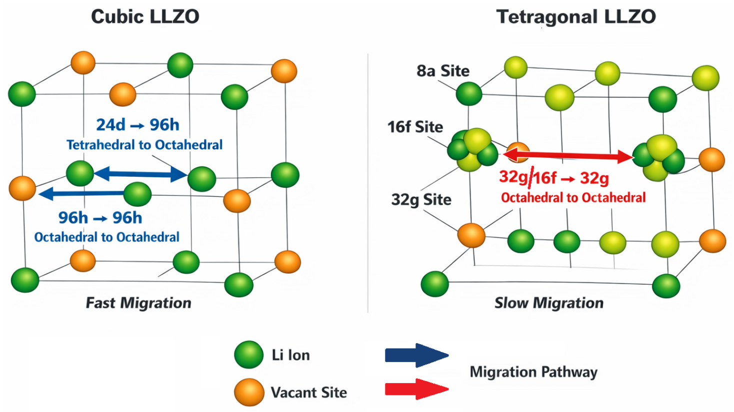

Figure 7. Differences in migration pathways between cubic LLZO and tetragonal LLZO.

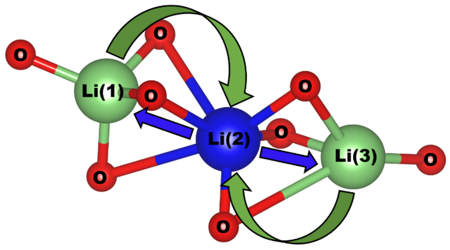

Figure 8. Possible migration pathways that can be taken by Li(1), Li(2) and Li(3) are shown by arrows depending on the vacant position available. Note that for a successful jump, the neighboring destination site must be vacant.

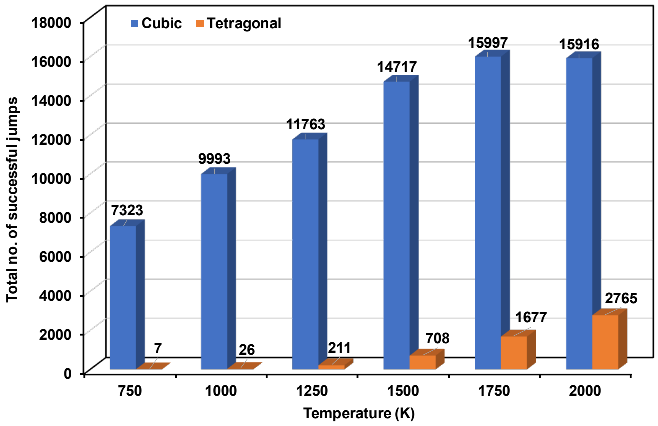

Figure 9. Total number of successful transitions at different temperatures during MD simulation.

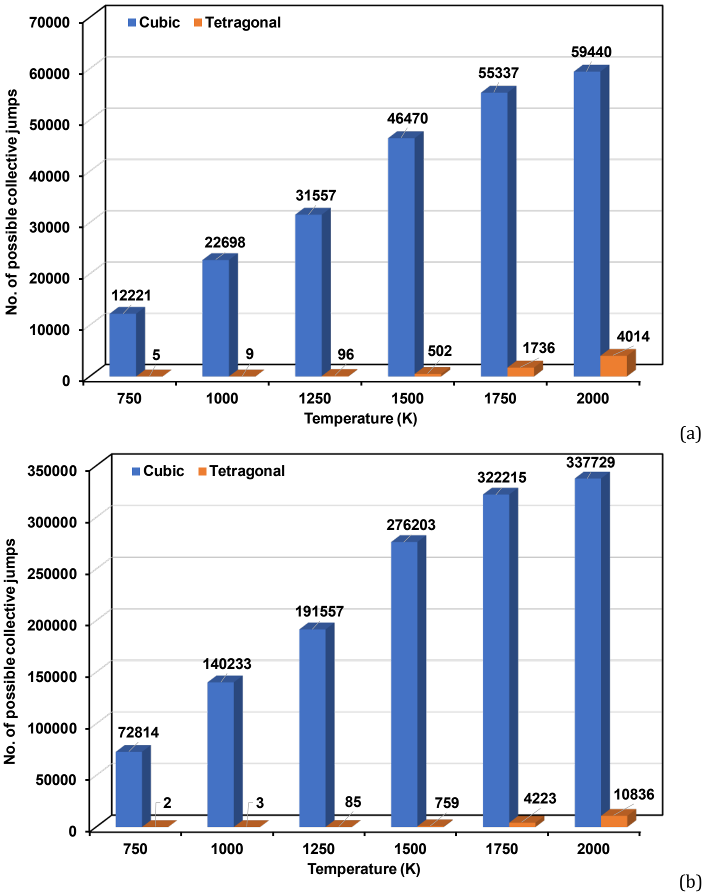

Figure 10. Total number of (a) possible collective jumps and (b) solo jumps at different temperatures during the MD simulations.

The sustained and frequent hopping in the cubic phase reflects its disordered lithium sublattice and abundant vacant sites, which promote continuous diffusion. In contrast, the tetragonal phase shows intermittent and significantly fewer jump events, indicating restricted ion mobility due to its ordered and fully occupied lithium framework. These results are in good agreement with previous molecular dynamic and AIMD investigations, which reported synchronized lithium-ion motion in the ordered tetragonal phase and more asynchronous individual hopping behavior in cubic LLZO [43].

Spatial maps of lithium-ion jump densities and migration pathways at 1500 K are shown in Figures S5 and S6 for cubic and tetragonal LLZO, respectively. Cubic LLZO exhibits frequent 24d ↔ 96h and 96h ↔ 96h transitions, forming an interconnected three-dimensional migration network that supports continuous lithium diffusion. In contrast, tetragonal LLZO shows predominantly 16f ↔ 32g transitions with limited long-range hopping, reflecting its ordered and fully occupied lithium sublattice. These differences highlight the structural origin of enhanced ionic mobility in the cubic phase. These maps clearly demonstrate a significantly higher density of migration pathways in cubic LLZO. Furthermore, the observed pathways form interconnected loop-like networks, in agreement with experimental and computational observations reported by Awaka *et al.* [7]. Such loop structures further enhance the long-range lithium-ion transport mechanism in the cubic phase.

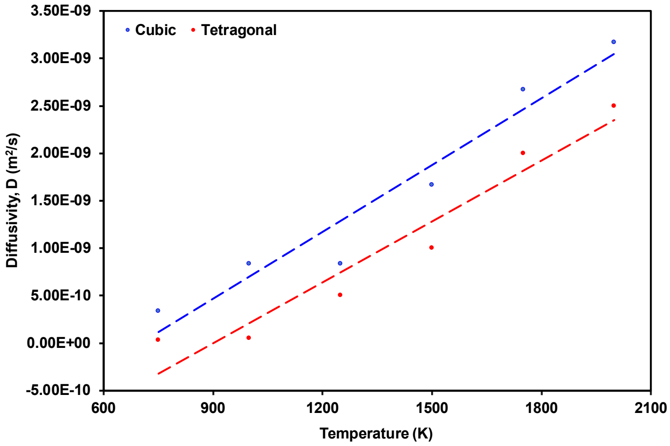

Figure 11. Li ion diffusivity of cubic LLZO and tetragonal LLZO at different temperatures.

The temperature dependence of the lithium ion diffusivity, extracted from the MD trajectories, is shown in Figure 11. In both phases, the diffusivity increases monotonically with temperature. However, at all temperatures studied, the diffusivity of the cubic phase is dominantly higher than that of the tetragonal phase. This difference directly reflects the higher frequency of lithium ion hopping events observed in cubic LLZO, as discussed above.

At 1500 K, the cumulative displacement statistics further highlight the contrast between the two phases. In cubic LLZO, the shortest and longest migration distances covered by individual lithium ions during the simulation are 8.51 µm and 57.11 µm, respectively. In contrast, in tetragonal LLZO, the corresponding distances are 3.20 µm and 31.01 µm. The total distance traveled by all lithium ions during the simulation reaches approximately 1.36 mm in cubic LLZO, compared to 0.84 mm in tetragonal LLZO. Figure S7 shows that the total displacement of Li(54) increases progressively in cubic LLZO, reflecting continuous and frequent hopping events. In contrast, tetragonal LLZO shows intermittent step-like increases separated by plateau regions, indicating restricted and less frequent migration. These results highlight the structurally driven enhancement of lithium diffusion in the cubic phase. These substantial differences arise despite identical simulation conditions, underscoring the critical role of lattice geometry, site occupancy, and vacancy concentration in governing lithium-ion transport.

The AIMD results demonstrate that lithium-ion motion in cubic LLZO is significantly more facile than that in tetragonal LLZO due to the presence of abundant vacant sites, shorter intersite distances, and a disordered lithium sublattice. These structural features collectively reduce activation barriers and enable more frequent lithium-ion hopping, resulting in enhanced diffusivity and, ultimately, higher ionic conductivity.

3.3. Activation energy and ionic conductivity

Figure 12 presents the mean square displacement (MSD) of lithium ions as a function of simulation time at six different temperatures for both cubic and tetragonal LLZO. The MSD profiles reflect the extent of lithium ion migration during AIMD simulations and provide direct insight into temperature-dependent diffusion behavior. As expected, the slope of the MSD curves increases with temperature, indicating enhanced lithium-ion mobility at elevated temperatures.

The diffusion coefficients were calculated from the MSD data using Equations 10–12. Assuming Arrhenius behavior, the temperature dependence of the diffusion coefficient: $D(T) = D_0 \exp\left(-\frac{E_a}{k_B T}\right)$ where D_0 denotes pre-exponential factor and E_a is the activation energy for lithium-ion diffusion. Accordingly, a linear relationship is obtained by plotting $\ln(D)$ as a function of $1/T$ [33,34]. The Arrhenius plots for cubic and tetragonal LLZO are shown in Figure 13.

From the linear fits to the Arrhenius plots, the activation energies for lithium ion diffusion are determined to be approximately 0.23 eV for cubic LLZO and 0.50 eV for tetragonal LLZO. The significantly lower activation energy of cubic LLZO confirms that lithium-ion migration is energetically more favorable in the cubic phase. This result is consistent with the presence of disordered lithium sublattice, shorter intersite distances, and a higher concentration of vacant sites, all of which contribute to reduced migration barriers.

Lithium ion conductivity was determined from the diffusion coefficients derived from the AIMD simulations using Equation 13. By extrapolating the Arrhenius fits to room temperature (300 K), the ionic conductivity of cubic LLZO is estimated to be 2.38×10^{-3} S/cm, whereas tetragonal LLZO exhibits a much lower conductivity of 3.03×10^{-7} S/cm. These values are summarized in Table S1.

The calculated room temperature ionic conductivity of cubic LLZO is in good qualitative agreement with the experimentally reported values, which typically range from 10^{-4} to 10^{-3} S/cm [5,45-47]. On the contrary, the low conductivity obtained for tetragonal LLZO is consistent with its experimentally observed poor lithium-ion transport properties. The agreement between simulation and experiment validates the reliability of the AIMD approach used in this study for capturing lithium ion diffusion mechanisms in garnet-type solid electrolytes.

These results demonstrate that the markedly higher ionic conductivity of cubic LLZO originates from its lower activation energy for lithium-ion migration, which arises from structural disorder and the availability of energetically accessible diffusion pathways.

3.4. Interatomic distances

To further elucidate the microscopic origin of the distinct lithium-ion transport behavior in cubic and tetragonal LLZO, radial distribution function (RDF) analyses were performed using Li(1) as the reference ion. The RDF provides quantitative information on interatomic distances and local coordination environments, which directly influence lithium-ion migration pathways.

Figures 14a and 14c present the RDFs between the reference lithium ion and all surrounding atomic species for cubic and tetragonal LLZO, respectively.

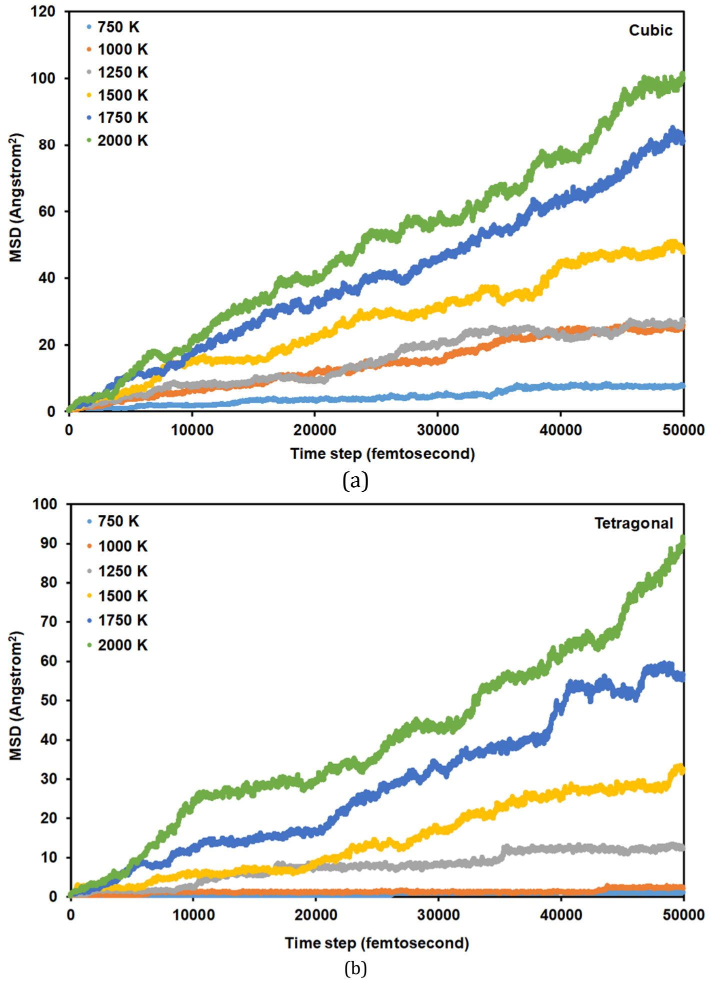

(a)

(b)

Figure 12. Mean square displacement (MSD) of Li ions at different temperatures during MD simulations in (a) cubic LLZO and (b) tetragonal LLZO.

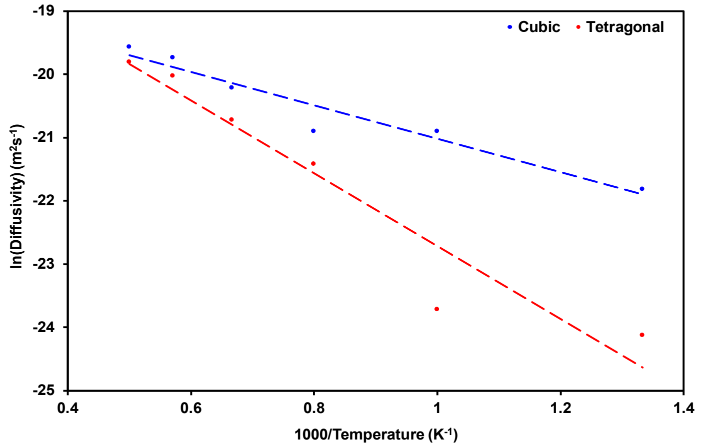

Figure 13. The Arrhenius plot depicts the logarithmic rate of the diffusion coefficient versus the inverse of the absolute temperature. The calculated diffusion coefficients at different temperatures are given in Table S1.

In both phases, the shortest interatomic distance corresponds to the Li–O bond, with a peak centered at approximately 1.60 Å. The second-nearest neighbors are lithium ions, appearing at distances of approximately 1.70 Å in cubic LLZO and 2.20 Å in tetragonal LLZO. Lanthanum and zirconium ions appear as the third- and fourth-nearest neighbors, respectively. These interatomic distances are in good agreement with previously reported structural studies [6,44].

Figures 14b and 14d show the Li–Li RDFs for cubic and tetragonal LLZO, respectively. In cubic LLZO, the jump distance histogram (Figure 6a) indicates that the majority of lithium-ion hopping events occur over distances of approximately 0.80 Å and 1.60 Å. However, the Li–Li RDF in Figure 14b does not show a peak below ~1.70 Å. This apparent discrepancy arises because two neighboring 96h sites in cubic LLZO are separated by less than 1.0 Å and cannot be simultaneously occupied by two lithium ions due to strong Coulombic repulsion [17].

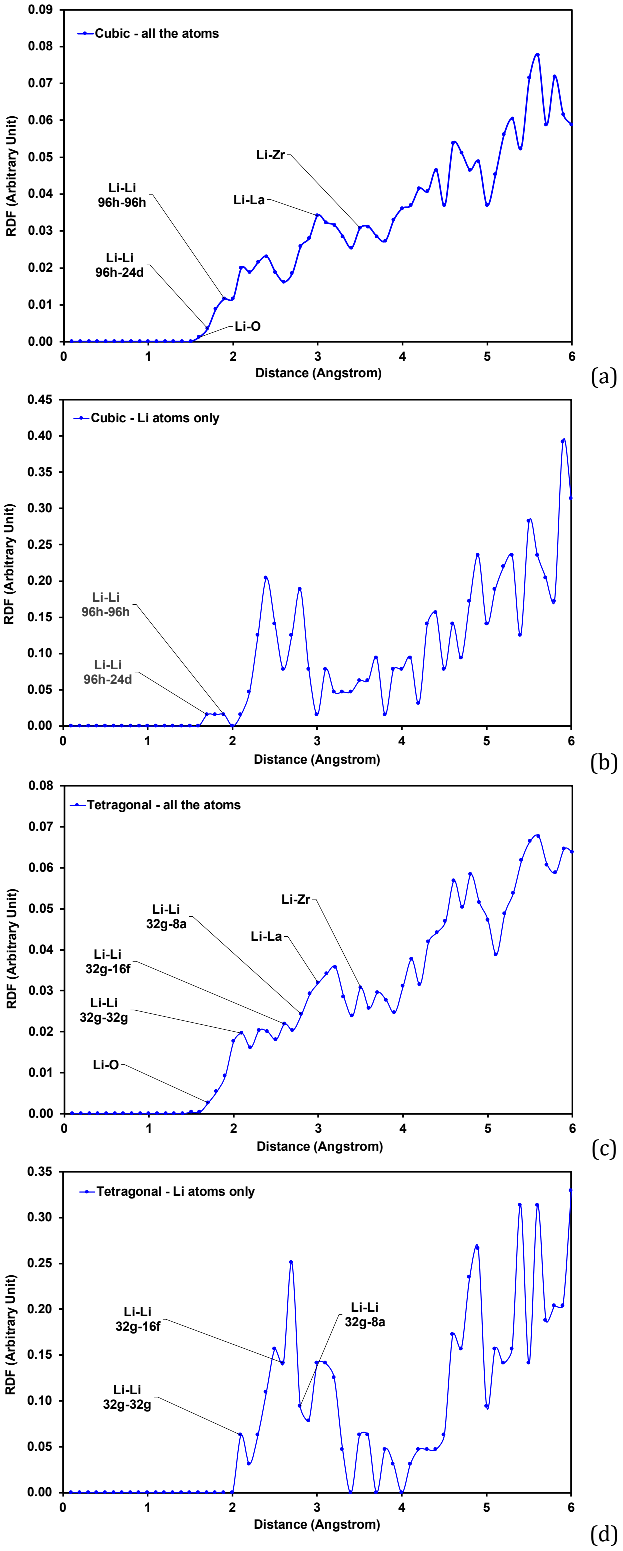

Figure 14. Radial distributions between all atoms (a), (c) and between Li-Li ions (b), (d), with respect to the reference Li(1) ion.

Consequently, although cubic LLZO provides 120 nominal lithium sites, not all of these sites can be occupied simultaneously. The Li–Li distance of approximately 1.80 Å corresponds to two lithium ions occupying 96h sites separated by an intervening vacant site.

In contrast, tetragonal LLZO exhibits a fully occupied and ordered lithium sublattice, in which lithium ions are sufficiently separated to minimize Coulombic repulsion. As a result, the lithium ion jump distances observed in Figure 6b are consistent with the Li–Li RDF shown in Figure 14d. The larger intersite distances and the lack of vacant sites significantly restrict lithium ion mobility in the tetragonal phase.

This RDF analysis reinforces the conclusion that lithium-ion transport in LLZO is strongly governed by site availability and intersite distances. In cubic LLZO, the combination of a partially occupied lithium sublattice, shorter effective hopping distances, and abundant vacancies enables frequent lithium-ion migration and low activation barriers. On the contrary, the ordered lithium arrangement and larger intersite separations in tetragonal LLZO hinder ion transport.

These observations suggest that reducing the lithium content in cubic LLZO, thereby increasing the number of vacant sites, is possible way to improve the ionic conductivity of LLZO. It can be achieved experimentally through aliovalent doping (e.g., with Al, Ga, Ta, or Rb), vacancy engineering, or the introduction of interstitial defects. Similarly, transforming the ordered lithium sublattice of tetragonal LLZO into a disordered configuration through dopant incorporation or high-temperature synthesis, which lead to stable cubic phase, may also be effective in improving the ionic conductivity of LLZO [6,16,17,48-51].

4. Conclusions

In this work, first-principles density functional theory and AIMD simulations were used to investigate the structural characteristics, lithium-ion migration mechanisms, and ionic conductivity of cubic LLZO and tetragonal LLZO. The results provide detailed atomistic insight into the fundamental origins of the markedly different lithium-ion transport properties observed in these two phases.

The simulations reveal that cubic LLZO possesses a highly disordered lithium sublattice with a large number of vacant interstitial sites, enabling frequent lithium ion hopping through interconnected migration pathways. In contrast, tetragonal LLZO exhibits a fully occupied and ordered lithium sublattice, which significantly restricts lithium-ion mobility and limits long-range diffusion. Analysis of lithium-ion trajectories, hopping statistics, and radial distribution functions demonstrate that shorter effective intersite distances and abundant vacancies in cubic LLZO substantially reduce the activation energy for lithium-ion migration.

Arrhenius analysis of temperature-dependent diffusion coefficients yields activation energies of approximately 0.23 eV for cubic LLZO and 0.50 eV for tetragonal LLZO. Similarly, the extrapolated ionic conductivity of cubic LLZO at room temperature is calculated to be 2.38×10^{-3} S/cm, is several orders of magnitude greater than that of the tetragonal phase and is consistent with reported experimental values. These findings confirm that structural disorder and vacancy concentration are the primary factors governing lithium-ion transport in garnet-type solid electrolytes.

The work highlights the critical role of lithium sublattice disorder in enhancing ionic conductivity and provides clear design guidelines for improving garnet-type solid electrolytes. Strategies such as aliovalent doping, vacancy engineering, and stabilization of the cubic phase are expected to be effective approaches for optimizing LLZO-based solid electrolytes for next-generation all-solid-state lithium batteries.

Future experimental validation of the theoretical predictions may involve exploring advanced doping strategies or defect engineering to enhance the disorder of lithium sublattice in cubic LLZO, thus effectively reducing the activation energy and increasing lithium ionic conductivity. Techniques such as multi-target reactive sputtering, multiple-source electron beam evaporation deposition, and atmosphere-controlled hot pressing may enable precise control over dopant concentration and defect density. In addition, extending atomistic modeling and simulations to grain boundaries, surfaces, and LLZO/anode and LLZO/cathode interfaces will be essential for further optimizing the material. These experimental and simulation efforts could further establish cubic LLZO as a highly competitive solid electrolyte for all-solid-state lithium-ion batteries.

Acknowledgements

Dmitri Kilin thanks the National Science Foundation CHE-1944921 for support of quantum dynamics methods development. Qifeng Zhang gratefully acknowledges the support from the US Army Combat Capabilities Development Command (DEVCOM) Ground Vehicle Systems Center (GVSC) and the National Center for Manufacturing Sciences (MCMS) (No. 2021021-142041, No. 2023167-142245). This work used resources of the Center for Computationally Assisted Science and Technology (CCAST) at North Dakota State University, which were made possible in part by National Science Foundation Major Research Instrumentation (MRI) Award No. 2019077.

Supporting information

The online version of this article contains supplementary material, which is available to authorized users.

Disclosure statement

Conflict of interest: The authors declare that they have no conflict of interest.
Data availability: Simulation data are available from the author on request.

CRediT authorship contribution statement

Conceptualization: Muhammad Mozammal Kamal Raju; Methodology: Muhammad Mozammal Kamal Raju; Software: Muhammad Mozammal Kamal Raju, Dmitri Kilin, Qifeng Zhang; Formal Analysis: Muhammad Mozammal Kamal Raju; Investigation: Muhammad Mozammal Kamal Raju; Resources: Dmitri Kilin, Qifeng Zhang; Data Curation: Muhammad Mozammal Kamal Raju; Writing - Original Draft: Muhammad Mozammal Kamal Raju; Writing - Review and Editing: Muhammad Mozammal Kamal Raju, Yulun Han, Dmitri Kilin, Yi Ding, Qifeng Zhang; Visualization: Muhammad Mozammal Kamal Raju, Dmitri Kilin, Qifeng Zhang; Funding acquisition: Dmitri Kilin, Qifeng Zhang; Supervision: Dmitri Kilin, Qifeng Zhang; Project Administration: Dmitri Kilin, Yi Ding, Qifeng Zhang.

ORCID and Email

Muhammad Mozammal Kamal Raju
mdmozammal.raju@ndsu.edu
https://orcid.org/0000-0003-1904-0523
Yulun Han
yulun.han@ndsu.edu
https://orcid.org/0000-0002-8619-0233
Dmitri Kilin
dmitri.kilin@ndsu.edu
https://orcid.org/0000-0001-7847-5549
Yi Ding
yi.ding8.civ@army.mil
Qifeng Zhang
qifeng.zhang@ndsu.edu
https://orcid.org/0000-0001-9386-4411

References

[1]. Armand, M.; Tarascon, J. Building better batteries. *Nature* **2008**, *451* (7179), 652–657.
[2]. Park, M.; Zhang, X.; Chung, M.; Less, G. B.; Sastry, A. M. A review of conduction phenomena in Li-ion batteries. *J. Power Sources* **2010**, *195* (24), 7904–7929.
[3]. Kerman, K.; Luntz, A.; Viswanathan, V.; Chiang, Y.; Chen, Z. Review—Practical Challenges Hindering the Development of Solid State Li Ion Batteries. *J. Electrochem. Soc.* **2017**, *164* (7), A1731–A1744.
[4]. Schipper, F.; Erickson, E. M.; Erk, C.; Shin, J.; Chesneau, F. F.; Aurbach, D. Review—Recent Advances and Remaining Challenges for Lithium Ion Battery Cathodes. *J. Electrochem. Soc.* **2016**, *164* (1), A6220–A6228.
[5]. Murugan, R.; Thangadurai, V.; Weppner, W. Fast Lithium Ion Conduction in Garnet-Type $Li_7La_3Zr_2O_{12}$. *Angew. Chem. Int. Ed.* **2007**, *46* (41), 7778–7781.
[6]. Awaka, J.; Kijima, N.; Hayakawa, H.; Akimoto, J. Synthesis and structure analysis of tetragonal $Li_7La_3Zr_2O_{12}$ with the garnet-related type structure. *J. Solid State Chem.* **2009**, *182* (8), 2046–2052.
[7]. Awaka, J.; Takashima, A.; Kataoka, K.; Kijima, N.; Idemoto, Y.; Akimoto, J. Crystal Structure of Fast Lithium-ion-conducting Cubic $Li_7La_3Zr_2O_{12}$. *Chem. Lett.* **2010**, *40* (1), 60–62.

[8]. Hong, H. Y.-P. Crystal structures and crystal chemistry in the system $Na_{1+x}Zr_2Si_xP_{3-x}O_{12}$. *Mater. Res. Bull.* **1976**, *11*, 173–182.

[9]. Ivanov-Schitz, A.; Bykov, A. B. Ionic conductivity of the $NaZr_2(PO_4)_3$ single crystals. *Solid State Ionics* **1997**, *100* (1-2), 153–155.

[10]. Bruce, P. G.; West, A. R. Phase diagram of the LISICON, solid electrolyte system, Li_4GeO_4-Zn_2GeO_4. *Mater. Res. Bull.* **1980**, *15*, 379–385.

[11]. Murayama, M.; Kanno, R.; Irie, M.; Ito, S.; Hata, T.; Sonoyama, N.; Kawamoto, Y. Synthesis of New Lithium Ionic Conductor Thio-LISICON—Lithium Silicon Sulfides System. *J. Solid State Chem.* **2002**, *168* (1), 140–148.

[12]. Thangadurai, V.; Weppner, W. Synthesis and Electrical Properties of K- and Pr-Substituted $LaGaO_3$ and $LaInO_3$ Perovskites. *J. Electrochem. Soc.* **2001**, *148* (12), A1294.

[13]. Birke, P.; Scharner, S.; Huggins, R. A.; Weppner, W. Electrolytic Stability Limit and Rapid Lithium Insertion in the Fast-Ion-Conducting Li0.29La0.57TiO3 Perovskite-Type Compound. *J. Electrochem. Soc.* **1997**, *144* (6), L167–L169.

[14]. Wolfenstine, J.; Allen, J. L.; Sumner, J.; Sakamoto, J. Electrical and mechanical properties of hot-pressed versus sintered $LiTi_2(PO_4)_3$. *Solid State Ionics* **2009**, *180* (14-16), 961–967.

[15]. Kuhn, A.; Narayanan, S.; Spencer, L.; Goward, G.; Thangadurai, V.; Wilkening, M. Li self-diffusion in garnet-type $Li_7La_3Zr_2O_{12}$ as probed directly by diffusion-induced Li7 spin-lattice relaxation NMR spectroscopy. *Phys. Rev. B.* **2011**, *83* (9), 094302.

[16]. Geiger, C. A.; Alekseev, E.; Lazic, B.; Fisch, M.; Armbruster, T.; Langner, R.; Fechtelkord, M.; Kim, N.; Pettke, T.; Weppner, W. Crystal Chemistry and Stability of "$Li_7La_3Zr_2O_{12}$" Garnet: A Fast Lithium-Ion Conductor. *Inorg. Chem.* **2010**, *50* (3), 1089–1097.

[17]. Bernstein, N.; Johannes, M. D.; Hoang, K. Origin of the Structural Phase Transition in $Li_7La_3Zr_2O_{12}$. *Phys. Rev. Lett.* **2012**, *109* (20), 205702 https://doi.org/10.1103/PhysRevLett.109.205702

[18]. de Klerk, N. J.; van der Maas, E.; Wagemaker, M. Analysis of Diffusion in Solid-State Electrolytes through MD Simulations, Improvement of the Li-Ion Conductivity in β-Li_3PS_4 as an Example. *ACS. Appl. Energy. Mater.* **2018**, *1* (7), 3230–3242.

[19]. Meng, Q.; May, P. S.; Berry, M. T.; Kilin, D. Sequential hydrogen dissociation from a charged $Pt_{13}H_{24}$ cluster modeled by *ab initio* molecular dynamics. *Int. J. Quant. Chem.* **2012**, *112* (24), 3896–3903.

[20]. Meng, Q.; Chen, J.; Kilin, D. Proton reduction at surface of transition metal nanocatalysts. *Molecular Simulation* **2014**, *41* (1-3), 134–145.

[21]. Ghazanfari, S.; Han, Y.; Arshad, A.; Xia, W.; Kilina, S.; Kilin, D. Exploring Peptide Bond Formation Using Transition State Search and Wave Packet Dynamics. *J. Phys. Chem. Lett.* **2025**, *16* (27), 6968–6974.

[22]. Han, Y.; Hobbie, E. K.; Kilin, D. S. First-Principles Molecular Dynamics of Monomethylhydrazine and Nitrogen Dioxide. *J. Phys. Chem. Lett.* **2019**, *10* (10), 2394–2399.

[23]. Erickson, M.; Han, Y.; Rasulev, B.; Kilin, D. Molecular Dynamics Study of the Photodegradation of Polymeric Chains. *J. Phys. Chem. Lett.* **2022**, *13* (19), 4374–4380.

[24]. Erickson, M.; Casañola-Martin, G.; Han, Y.; Rasulev, B.; Kilin, D. Relationships between the Photodegradation Reaction Rate and Structural Properties of Polymer Systems. *J. Phys. Chem. B.* **2024**, *128* (9), 2190–2200.

[25]. Chen, J.; Meng, Q.; Stanley May, P.; Berry, M. T.; Kilin, D. S. Time-dependent excited-state molecular dynamics of photodissociation of lanthanide complexes for laser-assisted metal-organic chemical vapour deposition. *Molecular Physics* **2013**, *112* (3-4), 508–517.

[26]. Han, Y.; Meng, Q.; Rasulev, B.; May, P. S.; Berry, M. T.; Kilin, D. S. Photofragmentation of the Gas-Phase Lanthanum Isopropylcyclopentadienyl Complex: Computational Modeling vs Experiment. *J. Phys. Chem. A.* **2015**, *119* (44), 10838–10848.

[27]. Han, Y.; Meng, Q.; Rasulev, B.; May, P. S.; Berry, M. T.; Kilin, D. S. Photoinduced Charge Transfer versus Fragmentation Pathways in Lanthanum Cyclopentadienyl Complexes. *J. Chem. Theory. Comput.* **2017**, *13* (9), 4281–4296.

[28]. Han, Y.; Anderson, K.; Hobbie, E. K.; Boudjouk, P.; Kilin, D. S. Unraveling Photodimerization of Cyclohexasilane from Molecular Dynamics Studies. *J. Phys. Chem. Lett.* **2018**, *9* (15), 4349–4354.

[29]. Granlie, J. D.; Hobbie, E. K.; Kilin, D. S. Formation and Luminescence of Single Oxygen Impurities on the Surface of SiC Nanocrystals. *J. Phys. Chem. Lett.* **2023**, *14* (26), 6202–6208.

[30]. Kohn, W.; Sham, L. J. Self-Consistent Equations Including Exchange and Correlation Effects. *Phys. Rev.* **1965**, *140* (4A), A1133–A1138.

[31]. Perdew, J. P.; Ernzerhof, M.; Burke, K. Rationale for mixing exact exchange with density functional approximations. *J. Chem. Phys.* **1996**, *105* (22), 9982–9985.

[32]. Perdew, J. P.; Burke, K.; Ernzerhof, M. Generalized Gradient Approximation Made Simple. *Phys. Rev. Lett.* **1996**, *77* (18), 3865–3868.

[33]. Laidler, K. J. The development of the Arrhenius equation. *J. Chem. Educ.* **1984**, *61* (6), 494.

[34]. Laidler, K. J. A glossary of terms used in chemical kinetics, including reaction dynamics (IUPAC Recommendations 1996). *Pure Appl. Chem.* **1996**, *68* (1), 149–192.

[35]. Kresse, G.; Furthmüller, J. Efficient iterative schemes for *ab initio* total-energy calculations using a plane-wave basis set. *Phys. Rev. B.* **1996**, *54* (16), 11169–11186.

[36]. Kresse, G.; Furthmüller, J. Efficiency of ab-initio total energy calculations for metals and semiconductors using a plane-wave basis set. *Comput. Mater. Sci.* **1996**, *6*, 15–50.

[37]. Blöchl, P. E. Projector augmented-wave method. *Phys. Rev. B.* **1994**, *50* (24), 17953–17979.

[38]. Perdew, J. P.; Burke, K.; Ernzerhof, M. Generalized Gradient Approximation Made Simple [Phys. Rev. Lett. 77, 3865 (1996)]. *Phys. Rev. Lett.* **1997**, *78* (7), 1396–1396.

[39]. Gražulis, S.; Chateigner, D.; Downs, R. T.; Yokochi, A. F.; Quirós, M.; Lutterotti, L.; Manakova, E.; Butkus, J.; Moeck, P.; Le Bail, A. Crystallography Open Database – an open-access collection of crystal structures. *J. Appl. Crystallogr.* **2009**, *42* (4), 726–729.

[40]. Materials Project. mp-942733: $Li_7La_3Zr_2O_{12}$ (Tetragonal, I4_1/acd, 142). https://next-gen.materialsproject.org/materials/mp-942733 https://doi.org/10.17188/1313215 (accessed Feb 10, 2026).

[41]. Zhang, Y.; Chen, F.; Li, J.; Zhang, L.; Gu, J.; Zhang, D.; Saito, K.; Guo, Q.; Luo, P.; Dong, S. Regulation mechanism of bottleneck size on Li^+ migration activation energy in garnet-type $Li_7La_3Zr_2O_{12}$. *Electrochimica. Acta.* **2018**, *261*, 137–142.

[42]. Wu, J.; Pang, W. K.; Peterson, V. K.; Wei, L.; Guo, X. Garnet-Type Fast Li-Ion Conductors with High Ionic Conductivities for All-Solid-State Batteries. *ACS. Appl. Mater. Interfaces.* **2017**, *9* (14), 12461–12468.

[43]. Meier, K.; Laino, T.; Curioni, A. Solid-State Electrolytes: Revealing the Mechanisms of Li-Ion Conduction in Tetragonal and Cubic LLZO by First-Principles Calculations. *J. Phys. Chem. C.* **2014**, *118* (13), 6668–6679.

[44]. Geiger, C. A.; Alekseev, E.; Lazic, B.; Fisch, M.; Armbruster, T.; Langner, R.; Fechtelkord, M.; Kim, N.; Pettke, T.; Weppner, W. Crystal chemistry and stability of "$Li_7la_3Zr_2O_{12}$" garnet: A fast lithium-ion conductor. *Inorg. Chem.* **2011**, *50*, 1089–1097.

[45]. Buschmann, H.; Dölle, J.; Berendts, S.; Kuhn, A.; Bottke, P.; Wilkening, M.; Heitjans, P.; Senyshyn, A.; Ehrenberg, H.; Lotnyk, A.; Duppel, V.; Kienle, L.; Janek, J. Structure and dynamics of the fast lithium ion conductor "$Li_7La_3Zr_2O_{12}$". *Phys. Chem. Chem. Phys.* **2011**, *13* (43), 19378.

[46]. Kokal, I.; Somer, M.; Notten, P.; Hintzen, H. Sol–gel synthesis and lithium ion conductivity of $Li_7La_3Zr_2O_{12}$ with garnet-related type structure. *Solid State Ionics* **2011**, *185* (1), 42–46.

[47]. Kalita, D.; Lee, S.; Lee, K.; Ko, D.; Yoon, Y. Ionic conductivity properties of amorphous Li–La–Zr–O solid electrolyte for thin film batteries. *Solid State Ionics* **2012**, *229*, 14–19.

[48]. Miara, L. J.; Richards, W. D.; Wang, Y. E.; Ceder, G. First-Principles Studies on Cation Dopants and Electrolyte|Cathode Interphases for Lithium Garnets. *Chem. Mater.* **2015**, *27* (11), 4040–4047.

[49]. Klenk, M.; Lai, W. Local structure and dynamics of lithium garnet ionic conductors: tetragonal and cubic $Li_7La_3Zr_2O_7$. *Phys. Chem. Chem. Phys.* **2015**, *17* (14), 8758–8768.

[50]. Raju, M. M.; Altayran, F.; Johnson, M.; Wang, D.; Zhang, Q. Crystal Structure and Preparation of $Li_7La_3Zr_2O_{12}$ (LLZO) Solid-State Electrolyte and Doping Impacts on the Conductivity: An Overview. *Electrochem.* **2021**, *2* (3), 390–414.

[51]. KC, S.; Longo, R. C.; Xiong, K.; Cho, K. Point defects in garnet-type solid electrolyte (c-$Li_7La_3Zr_2O_{12}$) for Li-ion batteries. *Solid State Ionics* **2014**, *261*, 100–105.